

Article

# Mini N<sub>2</sub>-Raman Lidar Onboard Ultra-Light Aircraft for Aerosol Measurements: Demonstration and Extrapolation

Patrick Chazette \*  and Julien Totems \*

Laboratoire des Sciences du Climat et de l'Environnement, Laboratoire mixte CEA-CNRS-UVSQ, CEA Saclay, 91191 Gif-sur-Yvette, France

\* Correspondence: patrick.chazette@lsce.ipsl.fr (P.C.); julien.totems@lsce.ipsl.fr (J.T.)

Received: 8 September 2017; Accepted: 22 November 2017; Published: 28 November 2017

**Abstract:** Few airborne aerosol research experiments have deployed N<sub>2</sub>-Raman Lidar despite its capability to retrieve aerosol optical properties without ambiguity. Here, we show the high scientific potential of this instrument when used with specific flight plans. Our demonstration is based on (i) a field-experiment conducted in June 2015 in southern France, involving a N<sub>2</sub>-Raman Lidar embedded on an ultra-light aircraft (ULA); and (ii) an appropriate algorithmic approach using two-level flight levels, aiming to solve the notorious instability of the airborne Lidar inversion for the retrieval of aerosol optical properties. The Lidar measurements include the determination of the aerosol extinction coefficient along ~500 m horizontal line of sight, and this value is used as a reference to validate the proposed algorithm. The Lidar-derived vertical profiles obtained during the flights are used as an input in a Monte Carlo simulation in order to compute the error budget in terms of biases and standard deviations on the retrieved aerosol extinction coefficient profile, as well as the subsequent optical thickness. The influence of the Lidar ratio (i.e., between aerosol extinction and backscatter) on the error budget is further discussed. Finally, from this end-to-end modeling, an optimal N<sub>2</sub>-Raman Lidar is proposed for airborne experiments, adapted to both small and large carriers.

**Keywords:** N<sub>2</sub>-Raman Lidar; ultra-light aircraft; airborne; aerosol; optical properties; simulator; error budget

---

## 1. Introduction

Atmospheric aerosol is a driver of air quality and climate change. However, it is one of the least known components of the atmospheric radiative balance, as already pointed out by the Intergovernmental Panel on Climate Change [1], as well as several decades' worth of scientific investigations [2]. Its main physical and chemical properties, and their spatiotemporal evolutions, need a better experimental characterisation to help improve regional models [3–7].

The characterisation of atmospheric aerosols must be carried out on spatiotemporal scales representative of their lifetime in the atmosphere, and allow for the best constraint of mesoscale models. Airborne measurements are powerful tools to this end, and, in the past, numerous major international field campaigns using airborne Lidar measurements, including campaigns on a regional scale, were conducted worldwide. For instance: (i) the Smoke/Sulfates, Clouds and Radiation—Brazil (SCAR-B) field-campaign over the Amazonia in 1995 [8]; (ii) the Tropospheric Aerosol Radiative Forcing Observational Experiment (TARFOX) over the US East coast in 1996 [9]; (iii) the International Global Atmospheric Chemistry (IGAC) field-campaign, which initiated a series of Aerosol Characterization Experiments (ACEs) including ACE-II in 1997 over the NE Atlantic Ocean [10]; (iv) the Arabian Sea and Indian Ocean off India with the INDIan Ocean EXperiment (INDOEX) in 1999 [11]; (v) the Simulation

de la Qualité de l'air en Ile-de-France (ESQUIF) and the Megacities: Emissions, urban, regional and Global Atmospheric POLLution and climate effects, and Integrated tools for assessment and mitigation (MEGAPOLI) over Paris in 2000 and 2009 [6,12,13]; (vi) the African Monsoon Multidisciplinary Analysis—Atmospheric Chemistry (AMMA-AC) over the tropical Africa in 2006 [14–16]; (vii) the Dust and Biomass-burning Experiment (DABEX) field-campaign over the West Africa in 2006 [17]; (viii) the Megacity Initiative: Local And Global Research Observations (MILAGRO) over the Mexico megalopolis in 2006 [18,19]; and (ix) the Polar Study using Aircraft, Remote Sensing, Surface Measurements and Models, Climate, Chemistry, Aerosols and Transport (POLARCAT) in 2008 [20]. To these coordinated field campaigns, we can add the airborne Lidar observations in response to crisis situations like the closing of the European airspace following the Eyjafjallajökull eruption in Iceland in April and May 2010 [21,22].

During these campaigns, Lidar measurements were used to follow the evolution of aerosols in the atmospheric column on a regional scale, and provide a near 3D vision of particle plumes. However, most of the Lidar systems used did not include  $N_2$ -Raman channels, which allow the simultaneous assessment of the extinction and backscatter coefficient of atmospheric aerosols, as permitted using a high spectral resolution Lidars [23]. Few studies have been performed with embedded Raman systems on aircrafts. All were focused on the measurement of the water vapor mixing ratio [24–26]. Methane and temperature were also measured by Heaps and Burris [24]. The only study dealing with aerosol measurements uses the  $N_2$ -Raman channel to directly estimate the aerosol backscatter coefficient [26].

In this paper, we present an evaluation of the scientific interest of a  $N_2$ -Raman Lidar to measure the vertical profile of aerosol properties in the low and middle troposphere from a light aircraft. The use of such a carrier mitigates the cost and difficulty of studies coupling a field campaign and an end-to-end model, as in Shang and Chazette [27]. Because the inversion of the elastic backscatter Lidar signal can be difficult to perform, lacking a perfect molecular reference as one of the boundary conditions to solve the Lidar equation [22], another approach is proposed. We show that an  $N_2$ -Raman Lidar can help constrain the mathematically unstable solution of the “top-down” Lidar equation [28]. We evaluate the associated uncertainties using a Monte Carlo simulation, and extrapolate the capabilities of a full-scale airborne system.

In Section 2, the method used to invert the airborne Lidar profiles is presented along with the strategy and flight plans as well as the instrumental tools. The field experiment is described in Section 3, the proposed method is applied on several airborne Lidar profiles and retrievals are compared to more direct horizontal measurements. Section 4 presents the error budget assessed using a complete Monte Carlo approach, evaluating the bias and standard deviation on the retrievals of Section 3 and extrapolating them to larger Raman Lidar systems dedicated to airborne measurements aboard scientific planes. The conclusions are given in Section 5.

## 2. Method

### 2.1. Theory

#### 2.1.1. Problem

To solve the backscatter Lidar equation for aerosol optical properties (aerosol extinction or backscatter coefficient, AEC or ABC), the classical approach presented by Klett [29] is generally used. It is based on the inversion of an integro-differential equation [30]. For Lidar measurements at nadir, as for zenith measurements, a reference altitude is required where the Lidar signal can be normalized to a known value. Nevertheless, it is not always easily obtained during airborne measurements. A reference altitude corresponding to pure molecular scattering is most often expected, but, in several situations, the atmosphere is not aerosol free at the flight altitude. This is even truer for airborne Lidar measurements because the reference signal is usually taken near the aircraft. In this “top-down” case, in contrast to the stable analytical solution given in Klett [28], the elastic integro-differential Lidar equations to be solved is unstable. However, the total or partial aerosol optical thickness (AOT)

derived from a N<sub>2</sub>-Raman channel [31], when available, can be used as a constraint to invert the Lidar equation [6,32]. Both the reference (close to the aircraft) and the constraint (far from the aircraft) provided by the N<sub>2</sub>-Raman channel helps to stabilize the solution. The precision on the restitution of the aerosol optical properties is closely linked to the AOT constraint uncertainty.

In the presence of aerosol at the reference altitude, close to the flight altitude, a method using nadir profiles obtained during ascent or descent has already been proposed by Chazette [33]. It remains difficult to apply in the lower tropospheric layers, under ~1 km agl. We will show in the following that the use of the N<sub>2</sub>-Raman-derived AOT at two altitude ranges, combined with specific flight plans, makes it possible to perform a Lidar profile inversion between the ground-level and the flight altitude.

### 2.1.2. Lidar Signals: Basic Equations

Hereafter, the Lidar signals are assumed to be corrected from both the solar background and the molecular transmission. Considering a flight altitude  $z_s$  and a profile index  $i$ , linked to the location of the ultra-light aircraft (ULA), the range-corrected Lidar signals, for both the elastic ( $S_i^E$ ) and the N<sub>2</sub>-Raman ( $S_i^N$ ) channels, are given as a function of altitude  $z$  by Measures [30]:

$$\left\{ \begin{array}{l} S_i^E = C_E \times F_E(z) \times (\beta_m(z) + \beta_a(z)) \times \overbrace{e^{-\frac{2}{\mu_i} \times AOT(z, z_s)}}^{\text{Aerosol transmission term}}, \\ S_i^N = C_N \times F_N(z) \times \beta_N(z) \times e^{-\frac{\epsilon}{\mu_i} \times AOT(z, z_s)} \end{array} \right. , \quad (1)$$

where  $\epsilon = \left(1 + \left(\frac{386.63}{354.67}\right)^{-A(z)}\right)$ , with  $A$  the aerosol Ångström exponent.  $C_E$  ( $C_N$ ) is the system constant and  $F_E$  ( $F_N$ ) is the overlap function for the elastic (N<sub>2</sub>-Raman) channel. The molecular and aerosol backscatter coefficient (ABC) are  $\beta_m$  and  $\beta_a$ , respectively. The N<sub>2</sub>-Raman backscatter signal is  $\beta_N$ . The cosine of the pointing angle is  $\mu_i$ . The aerosol optical thickness (AOT) at 355 nm between  $z$  and  $z_s$  is given as a function of the AEC  $\alpha_a$  as

$$AOT(z, z_s) = \int_z^{z_s} \alpha_a(z') \times dz'. \quad (2)$$

Given the molecular density profile derived from meteorological measurements (pressure and temperature) on the aircraft, the N<sub>2</sub>-Raman channel can be used to directly determine the AOT between two altitude levels. Note that the AEC and the ABC are linked via the Lidar ratio (LR), which is equal to the ratio between the AEC and the ABC. The AOT is assessed for these two different altitude ranges. The former, close to the flight altitude where the overlap factor is equal to 1, will be used as a reference. The latter, in the planetary boundary layer (PBL), will be a constraint for the inversion process via the aerosol transmission term, as shown in Royer et al. [34]. Such an approach offers the opportunity to retrieve simultaneously the vertical profile of the AEC under the aircraft and the equivalent LR in the altitude range where the inversion is performed. The LR is then assumed to be constant with altitude: this constitutes a rather strong hypothesis; however, it is necessary considering the measurement description (see Section 2.2). More details will be given in the following about the retrieval of the AOT from an N<sub>2</sub>-Raman embedded on an aircraft.

### 2.1.3. N<sub>2</sub>-Raman Lidar-Derived AOT

Due to the variation of the pointing angle with the ULA attitude, the geometric mean ( $S^N$ ) of the signal is preferred to an arithmetic mean in order to avoid signal distortion. Hence, after correction of the known N<sub>2</sub>-Raman backscatter signal  $\beta_N(z)$  and overlap factor  $F_N(z)$ , considering  $n$  Lidar profiles not very distant from each other:

$$S^N(z) = \sqrt[n]{\prod_{i=1}^n S_i^N(z)}. \quad (3)$$

They can be rewritten as

$$S^N(z) = C_N \times e^{-\varepsilon \times AOT(z, z_s) \times \sum_{i=1}^n \frac{1}{\mu_i}}. \quad (4)$$

Considering the ratio  $R(z) = S^N(z)/S^N(z_{up})$ , between two altitude levels  $z$  and  $z_{up}$  ( $z_{up} > z$ ), the AOT is given by:

$$AOT(z, z_{up}) = \frac{-\log(\prod_{i=1}^n R_i(z))}{\varepsilon \times \sum_{i=1}^n \frac{1}{\mu_i}}. \quad (5)$$

The calculation must also take into account the noise level on the N<sub>2</sub>-Raman signal. This requires a suitable smoothing, especially to estimate the reference near the flight altitude. We can then fit  $R(z)$  with an exponential function  $e^{-\frac{(z_{up}-z)}{H}}$  of height scale  $H$ . This is justified by the form of the ratio  $R(z) = e^{-\varepsilon \cdot \sum_{i=1}^n \frac{1}{\mu_i} \cdot (z_{up}-z) \cdot \bar{\alpha}}$ , where  $\bar{\alpha}$  is the mean AEC assumed to be constant between  $z$  and  $z_{up}$ .  $H$  is determined by a linear least square fitting on  $\log(R_i)$ .

#### 2.1.4. Other Useful Parameters

Before any inversion of the Lidar signal, it is necessary to identify the ground level with respect to the flight altitude and to calculate the overlap factors of the Lidar reception channels. The ground-echo is processed as presented in Shang et al. [35] for each mean Lidar profile to retrieve the former. The Lidar overlap factors for the elastic and N<sub>2</sub>-Raman channels can be retrieved using horizontal lines of sight during aircraft ascent or descent, as already performed from ground-level by Chazette [36]. The results are presented in Section 3.1.2.

#### 2.2. Strategy and Flight Plans

In order to assess the potential of a plane-embedded Raman Lidar system, we have used the Lidar for Atmospheric Surveys using Raman Scattering (LAASURS) Lidar initially developed for ground-based measurements [34]. For inexpensive testing, it is flown on an ULA vector, as in the AMMA international campaign [37], or the French campaign for the calibration and validation of CALIPSO [38]. The embedding of the Lidar has been modified to minimize the thermal effects of relative wind and reduce the payload weight.

Flight plans (Table 1) have been designed to estimate Lidar overlap factors and a reference profile of aerosol extinction coefficient via horizontally pointing measurements [37] as well as to constrain nadir pointing Lidar inversion. The pulse energy of the Lidar system remains insufficient for significant N<sub>2</sub>-Raman measurements between the ground and the altitude of the ULA when above ~1 km. Moreover, at the maximum ULA flight altitude in the mid-troposphere, a purely molecular scattering, which is used to normalize the Lidar profile before inversion, cannot always be inferred. A strict flight protocol (Figure 1) has thus been implemented during a meteorologically stable period in June 2015.

First, the flight plan comprises a slow spiral ascent (or descent) up to approximately 3 km above the mean sea level (amsl) (or from 3 km amsl to the ground). This altitude limitation is due to restrictions imposed by air traffic control over the campaign area. More generally, research aircrafts also often encounter such constraints due to local regulations or the presence of other onboard instruments. During this spiral phase, the Lidar is aiming horizontally. Once at the ceiling altitude, the Lidar is rotated to aim at the nadir. The ULA then flies successively at two altitude levels (high altitude/ceiling, and low altitude/PBL top) but above the same ground track, so as to measure roughly the same atmospheric volume. The low altitude stage, just above the PBL, uses Raman-derived AOT to constrain the inversion of the profiles acquired in the high-altitude stage. This measurement scenario assumes that the atmospheric content does not vary much between the two stages, which can be verified a posteriori by the evolution of measured optical properties during each stage. The variation will also be included in the error budget developed in Section 4.

The processing algorithm for this coupled Raman and elastic profile inversion can thus be tested and validated. These measurements also allow, thanks to a simulator prompted by the observed signals, to define the optimal characteristics of an airborne Lidar system. Such an instrument must be capable of restituting AEC vertical profiles on larger spatial scales while not being limited by the presence of aerosol at the flight altitude.

**Table 1.** Flight information: identification, date and description of flights performed.

Flight Identification	Date in June 2015 Local Time	Description
A	18th 1715–1810	Spiral between ground level (~350 m) and ~3.5 km above the mean sea level (amsl) with Nadir shooting during ascent and horizontal shooting during descent
B	22nd 2215–2300	Same as flight A
C	24th 1450–1740	Stage 1: spiral between ground level (~350 m) and ~3.2 km with Nadir shooting Stage 2: constant level flight above the Rhône valley at 3.2 km amsl Stage 3: half-turn to follow a constant level flight at ~1.3 km amsl above the same ground track as stage 2 Stage 4: descent for landing with horizontal shooting
D	24th 1840–2030	Stage 1: spiral between ground level (~350 m) and ~3.2 km with Nadir shooting Stage 2: constant level flight crossing the Rhône valley at 1.4 km amsl Stage 3: half-turn to follow a constant level flight at ~3.2 km amsl above the same ground track as stage 2 Stage 4: descent for landing with horizontal shooting

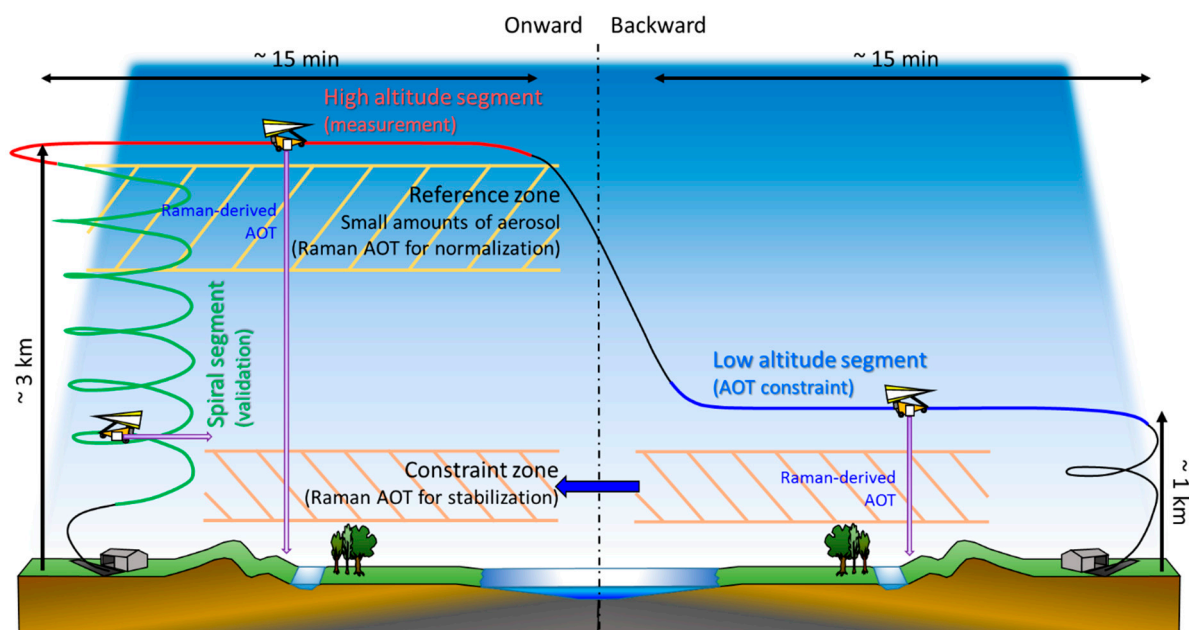


**Figure 1.** Schematic representation of the ideal flight plan to implement the inversion method described in Section 2.2.

### 2.3. Instrumental Tools

#### 2.3.1. Ultra-Light Aircraft

A Tanarg 912 S BioniX 15 ULA, built by the company Air Création (Aubenas, France), with a maximum total payload of approximately 250 kg including the pilot, was used for airborne measurements. Flight durations were 1–2 h, depending on flight conditions, with a cruise speed around 85–90 km·h<sup>-1</sup>. The ULA main flight characteristics are given in Table 2. For our experiment, the N<sub>2</sub>-Raman Lidar LAASURS was embedded on the ULA, along with a VAISALA 300 meteorological probe for temperature, pressure and relative humidity (Figure 2). These measurements are used to derive the molecular contribution to the Lidar signal. The ULA location was provided by a Global

Positioning System (GPS) and an Attitude and Heading Reference System (AHRS), which are part of the MTi-G components sold by XSens (Enschede, Netherlands) [39].



**Figure 2.** Tanarg 912 S BioniX 15 ultra-light aircraft (ULA). The airborne Lidar for atmospheric surveys using Raman Scattering (LAASURS) is embedded on the left side of the ULA.

**Table 2.** Tanarg 912 XS ultra-light aircraft (ULA) main flight characteristics.

ULA Flight Characteristics	
True airspeed: 17 to 40 m·s <sup>-1</sup> (60 to 145 km·h <sup>-1</sup> )	Endurance: 3 h (max 4 h at 20 m·s <sup>-1</sup> )
Ascent speed: up to 365 ft·min <sup>-1</sup> (110 m·min <sup>-1</sup> )	Maximum equipment payload: 120 kg
Descent speed: 825 ft·min <sup>-1</sup> (250 m·min <sup>-1</sup> )	Maximum altitude: 5.8 km

### 2.3.2. The N<sub>2</sub>-Raman Lidar

The N<sub>2</sub>-Raman Lidar LAASURS uses a frequency-tripled Nd:YAG (Neodymium-doped yttrium aluminum garnet) laser source at 355 nm with an emitted energy per pulse of 16 mJ. This Lidar system has been described and validated in Royer et al. [34], and more recently in Dieudonné et al. [40] and Chazette et al. [41]. As shown hereafter, its wide field-of-view (FOV) (~2.3 mrad) allows a full overlap of the transmission and reception paths beyond ~100–200 m. Three different channels are used to record the total, the cross-polarized (with respect to the laser emission) elastic backscatter signal of the atmosphere (elastic channels), and the inelastic nitrogen vibrational Raman backscattered signal (N<sub>2</sub>-Raman channel). The LAASURS instrument can be used in an airborne configuration with minimal restrictions, as it fulfills eye-safety requirements just 1 meter away from the system. The main characteristics of the Lidar are given in Table 3.

**Table 3.** Lidar for Atmospheric Surveys using Raman Scattering (LAASURS) main characteristics.

Laser	Nd:Yag	Emitted Energy		16 mJ	
Emitted wavelength	355 nm	Pulse repetition frequency		20 Hz	
Acquisition frequency	200 MHz	Native vertical sampling		0.75 m	
		Averaged on 400 profiles during flights at 90 km·h <sup>-1</sup>			
		Maximum range	Horizontal resolution	Vertical resolution	Temporal resolution
Reception channels	Elastic // 354.67 nm Elastic ⊥ 354.67 nm Raman-N <sub>2</sub> 386.63 nm	3 km 1.5 km 1 km	500 m	30 m	20 s
Field of view	~2.3 mrad	Total overlap		~200 m	
Reception diameter	15 cm	Spectral Bandwidth		0.3 nm	
Detector	Photomultiplier	Detection mode		Analog	
Weight	~45 kg	Power supply		500 W	

The LAASURS Lidar is fixed on to a rotatable arm on the side of the ULA. It can be pointed forward or towards nadir by the ULA pilot. The instrument is controlled by a custom Labview software on a

PXI (Peripheral Component Interconnect (PCI) eXtensions for Instrumentation) computer (National Instruments, Austin, TX, USA), allowing the continuous adaptation of detector gain to the background radiance. The power supply for the ULA payload is an alternator capable of delivering the required 600–700 W, thus making the system autonomous.

### 3. Experiment

The experiments took place over two separate stages over Ardèche and the Rhône valley (southeastern France). During the first phase (Section 3.1), airborne measurements allowed the evaluation of the overlap factors and the validation of the two methods used to retrieve vertical profiles of AEC, as described in Section 2.1. During the second phase (Section 3.2), the proposed algorithm was tested on flight plans similar to the one presented in Section 2.2.

#### 3.1. Ascendant Spiral Flight Phase

##### 3.1.1. Description

These flights are mainly dedicated to the evaluation of the overlap factor and the test of the proposed algorithm. Two flights were performed, the first during daytime and the second during nighttime, vertically from Aubenas airfield (44.54° N, 4.37° E) following the first part of the description shown on Figure 3, with the ULA spiraling up and down. First, between the ground and ~3.5 km amsl, the Lidar is aiming at the nadir to test the algorithm, and then it is aiming horizontally to assess the overlap factors and the vertical profile of AEC. Note that the angle spread around the desired line of sight remains small (under 2°) in all the considered cases; thus, the effect of projection remains small when comparing one profile to another.

The approach for this first series of flights is as follows: (i) assess the overlap factors; (ii) invert the horizontal measurements; (iii) calculate the AOTs both close to the flight altitude and in the PBL; and (vi) invert the nadir measurements and calculate the LR.

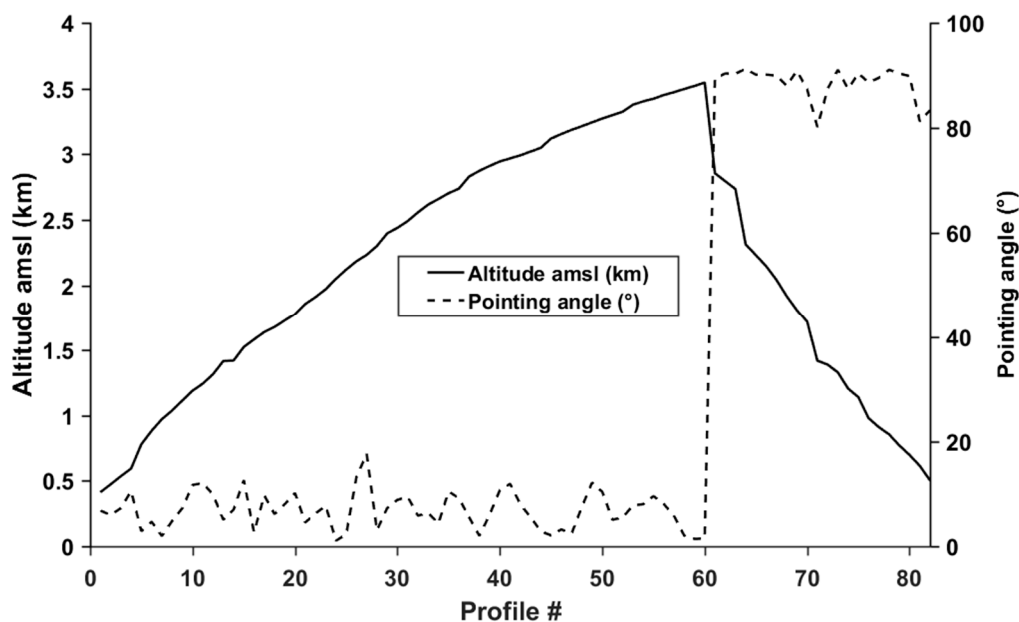


**Figure 3.** Flight profile altitude and the pointing angle for the flight A (18 June 2015), where the first 590 profiles are pointing down as the ULA rises, and the last 24 are pointing horizontal as the ULA descends. The nadir and horizontal phases are ~20 and ~7.5 min, respectively.

### 3.1.2. Overlap Factor

The overlap factor is assessed using an approach already described in Chazette [36]. The overlap factors of both the elastic and N<sub>2</sub>-Raman channels are given in Figure 4. They include the horizontal measurements of flights A and B. For the elastic channels (Figure 4a), the two flights give similar results with an overlap factor equal to 1 at a ~0.2 km distance from the emitter. This distance is reduced to ~0.1 km for the N<sub>2</sub>-Raman channel (Figure 4b). Flight A on 18th of June, performed during daytime, shows a higher level of noise than flight B, as could be expected.

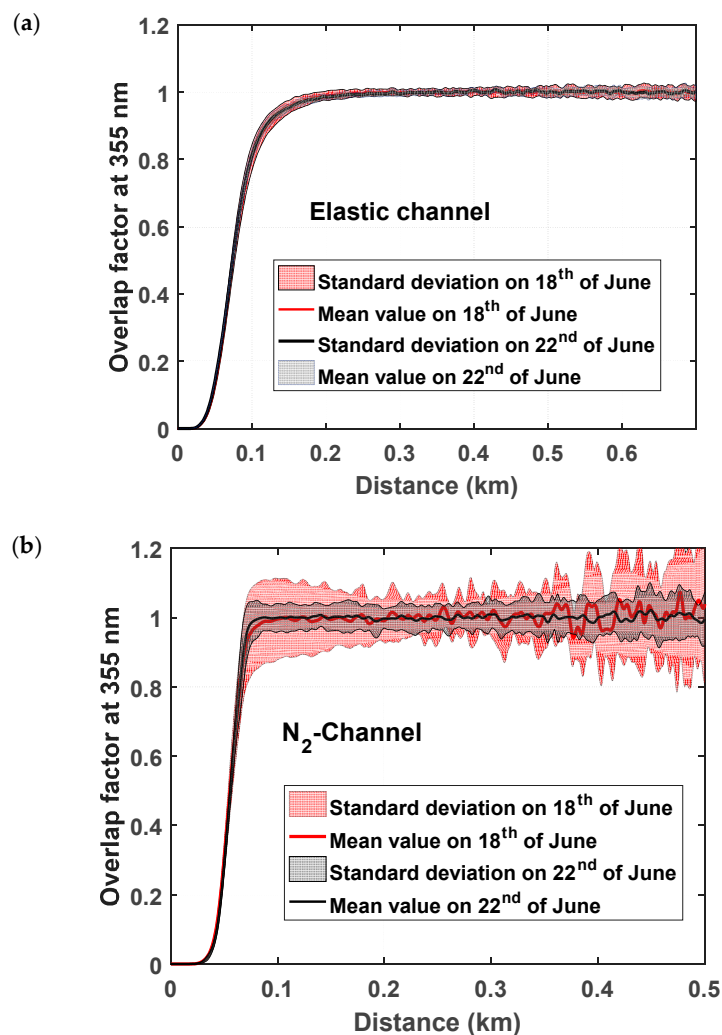


**Figure 4.** Overlap factor of (a) elastic channel; and (b) N<sub>2</sub>-Raman channel. The measurements were performed during the daytime on 18th of June (flight A) and the nighttime on 22nd of June (flight B).

### 3.1.3. Inversion from Horizontal Measurements

Horizontal measurements are inverted, as proposed by Chazette et al. [37], between ~0.3 and 0.8 km from the ULA. For flights A and B, vertical profiles of AEC obtained during the descent of the ULA are shown in Figure 5, as red lines, surrounded by an orange area representing uncertainty projected from the noise level. The final vertical resolution is only 250 m, so as to accumulate enough measurement points (red dots). This method using the elastic channel is mostly immune to sky background noise in the considered ~1 km range, as shown by the moderate dispersion of the results, which result from both noise-induced uncertainty and the natural variability of the atmosphere along the line of sight and within 250 m of strata. Note that the profiles retrieved using the N<sub>2</sub>-Raman channel

in the same horizontal setting during the nighttime show similar trends of AEC as in Figure 5, but with ~3 times higher root mean square (rms) error. During the daytime, measurements are impossible with this channel due to insufficient signal to noise ratio (SNR).

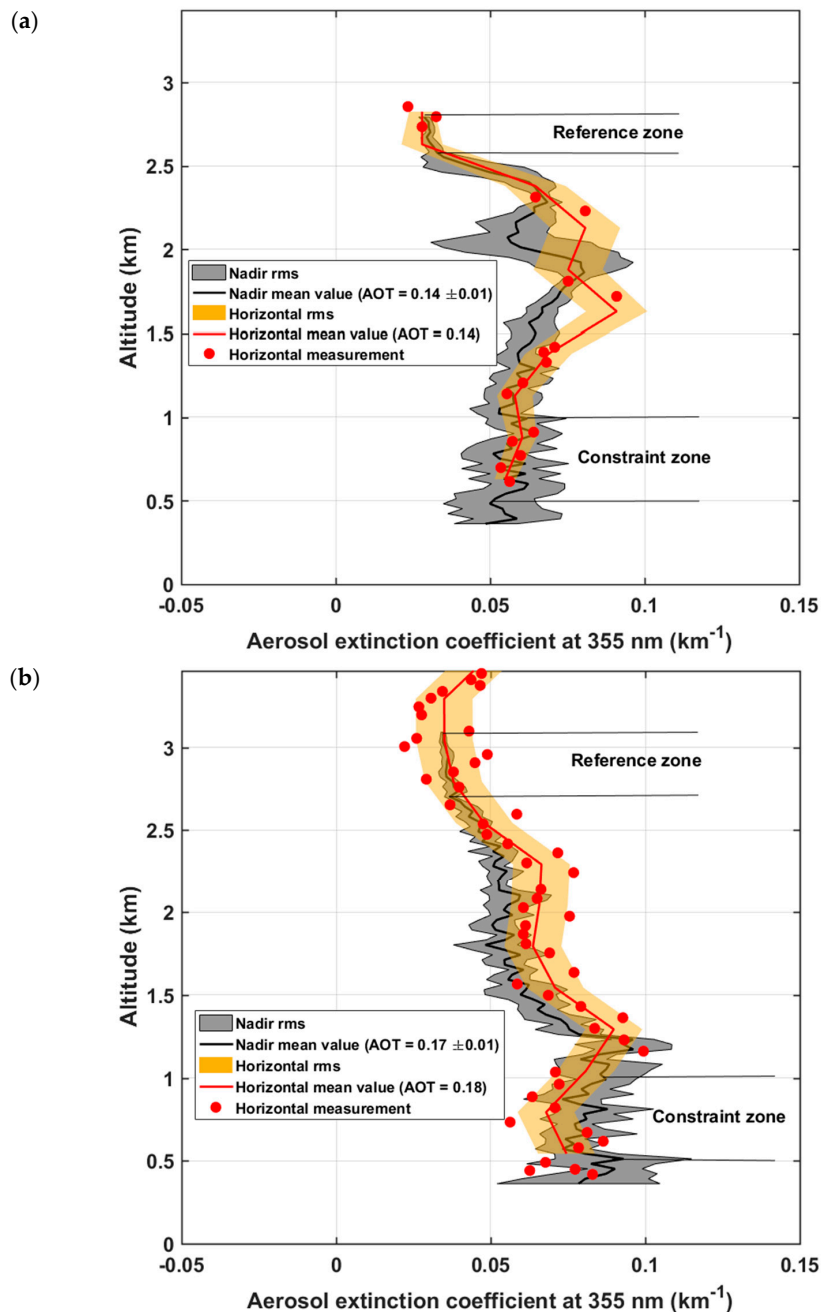


**Figure 5.** Vertical profiles of the aerosol extinction coefficient derived from the horizontal and nadir Lidar shootings for: (a) flight A on 18th of June for a planetary boundary layer (PBL) height of between 1.6 and 1.9 km above the mean sea level (amsl) and (b) flight B on 22nd of June for a PBL height of ~1.25 km amsl. The standard deviations are represented by the shaded areas. The nadir profiles are averaged over ~2 min. Each horizontal measurement of aerosol extinction coefficient is obtained over 20 s, between ~0.3 and 0.8 km from the ULA.

### 3.1.4. Inversion from Nadir Measurements

Nadir Lidar measurements, obtained from above the spiral described in the previous section, are then forward-inverted using AEC values from (i) the upper part of the profiles for normalization (between ~2.7 and 3 km amsl); and (ii) an additional constraint on AOT between 0.5 and 1 km amsl to match the integrated AEC measured in this layer, so as to set a value for LR. This allows to closely simulate the algorithm proposed in Section 2.1. The results are also presented in Figure 5, as black lines surrounded by grey areas for error. They are a very good match for the deduced AEC profiles and allow for deriving LR, which is here found to be around 35 and  $40 \pm 10$  sr for the two flights. The 10 sr error on this determination is mostly dependent on SNR. Because of this, the Lidar data is averaged over 30 m and nine vertical profiles (over which altitude is stable within less than 10 m) before the inversion, degrading resolution but yielding SNR ~10 at about 0.5 km amsl.

A large discrepancy exists between the retrieved values of AEC from horizontal and the nadir shots on flight A (18th of June, Figure 5a), as observed above 1.5 km amsl, and AEC from horizontal measurements are higher by about 35%. We attribute this to the strong variability of aerosol scattering properties around this altitude on this day. Indeed, between 1.5 and 3 km amsl, a dry layer possibly containing terrigenous particles can be identified, as shown in Figure 6. This layer is associated with relative humidity values below 40% between 2 and 2.5 km amsl. Volume depolarization ratio (VDR) is measured there to be 1.2%, corresponding to particle depolarization ratio (PDR) values between 4% and 5% (Chazette et al. [42] for the calculation method). At the base of this layer, the atmospheric instability has led to the formation of cumulus-type clouds, maybe facilitated by the presence of aerosols as condensation nuclei. During the daytime throughout the campaign, cumulus clouds have been observed above the Aubenas airfield, creating inhomogeneity along the flight, leading to a possible overestimation for horizontal measurements of the AEC in the lower free troposphere.

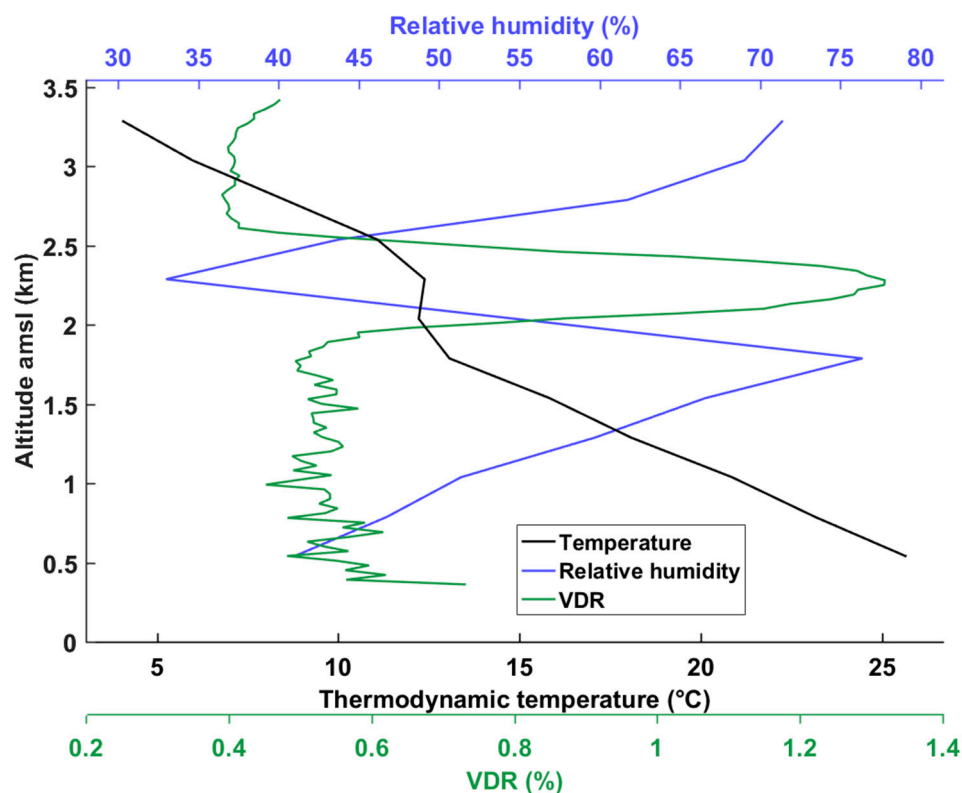


**Figure 6.** Vertical profiles of the relative humidity, temperature and volume depolarization ratio for the flight A on 18 June 2015.

### 3.2. Flights Using Two Altitude Stages

Flights along the paths described in Section 2.2 have been performed to implement the proposed algorithm. Two flights were performed on 24 June 2015, at the beginning and the end of the afternoon (Table 1). The relevant parts of the flights are identified on Figure 7, including stages around 3 and 1 km amsl. The Moderate Resolution Imaging Spectroradiometers (MODIS)-derived AOTs during these two flights (given by the Aqua and Terra satellites successively) are similar, about 0.07 at 550 nm. Because of air traffic restrictions, we were not able to perform low altitude flights next to the Mediterranean Coast where AOTs would have been stronger. This study was thus made in lower SNR conditions than expected. For higher SNRs, it will therefore also be relevant. Note that the Spinning Enhanced Visible and InfraRed Imager (SEVIRI)-derived AOTs are also given over sea in Figure 7.

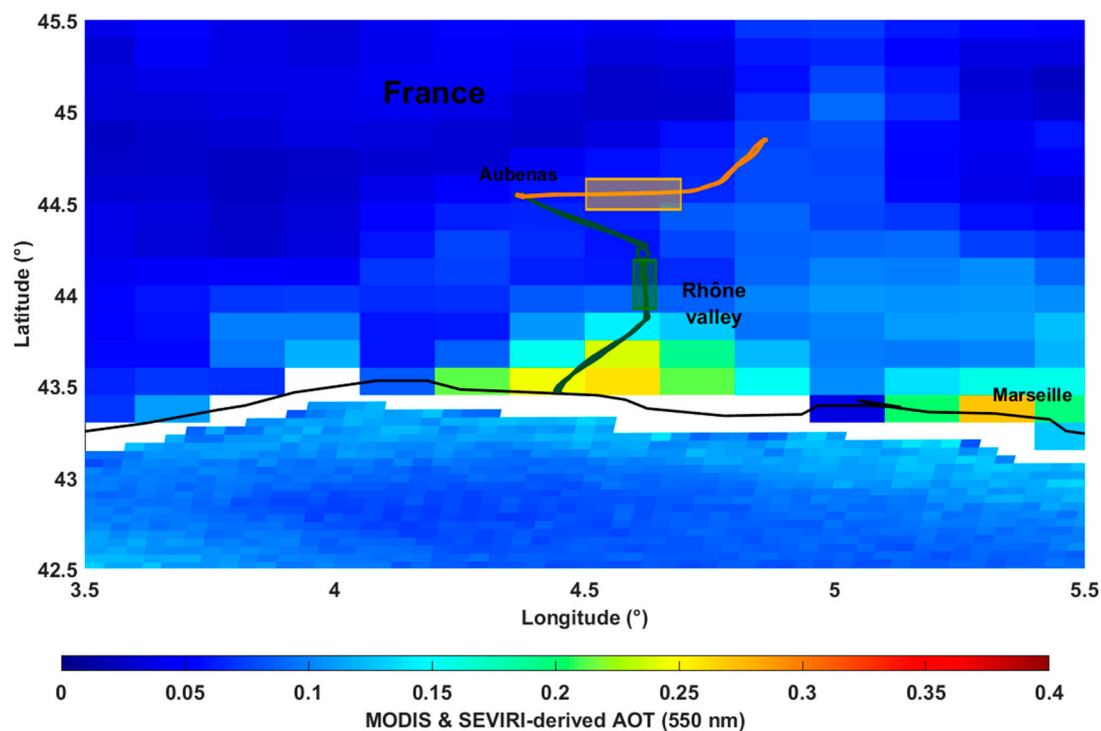


**Figure 7.** Ground-tracks of flights C (orange) and D (green) on 24 June 2015. The ground-tracks are superimposed to the aerosol optical thickness (AOT) at 550 nm derived by MODIS (over continent) and SEVIRI (over sea). The AOTs are computed between 10:00 a.m. and 2:00 p.m. UTC (universal time count). The framed areas represent the parts of the flight paths where the study is carried out.

#### 3.2.1. Flight Plan Descriptions

Flights C and D are presented in Figure 8 in terms of apparent aerosol backscatter coefficient ( $ABC_{app}$ )  $S_i^E$  given by Equation (1). They include the stages presented in Section 2.2, although they may not take place in the same order as in Figure 1. Each flight ends with a spiral descent with the Lidar aiming horizontally, allowing the evaluation of a vertical profile of AEC for comparison. The time when the ULA carrier starts flying back on its track is indicated by a vertical black line. The profiles and used altitude zones are highlighted in gray: between 0.5 and 1 km amsl for the constraint zone and between 2.35 and 2.85 km amsl for the reference zone. Values of  $ABC_{app}$  are higher when the flight altitude is low because of variations of laser energy with temperature, which will be discussed in Section 4.

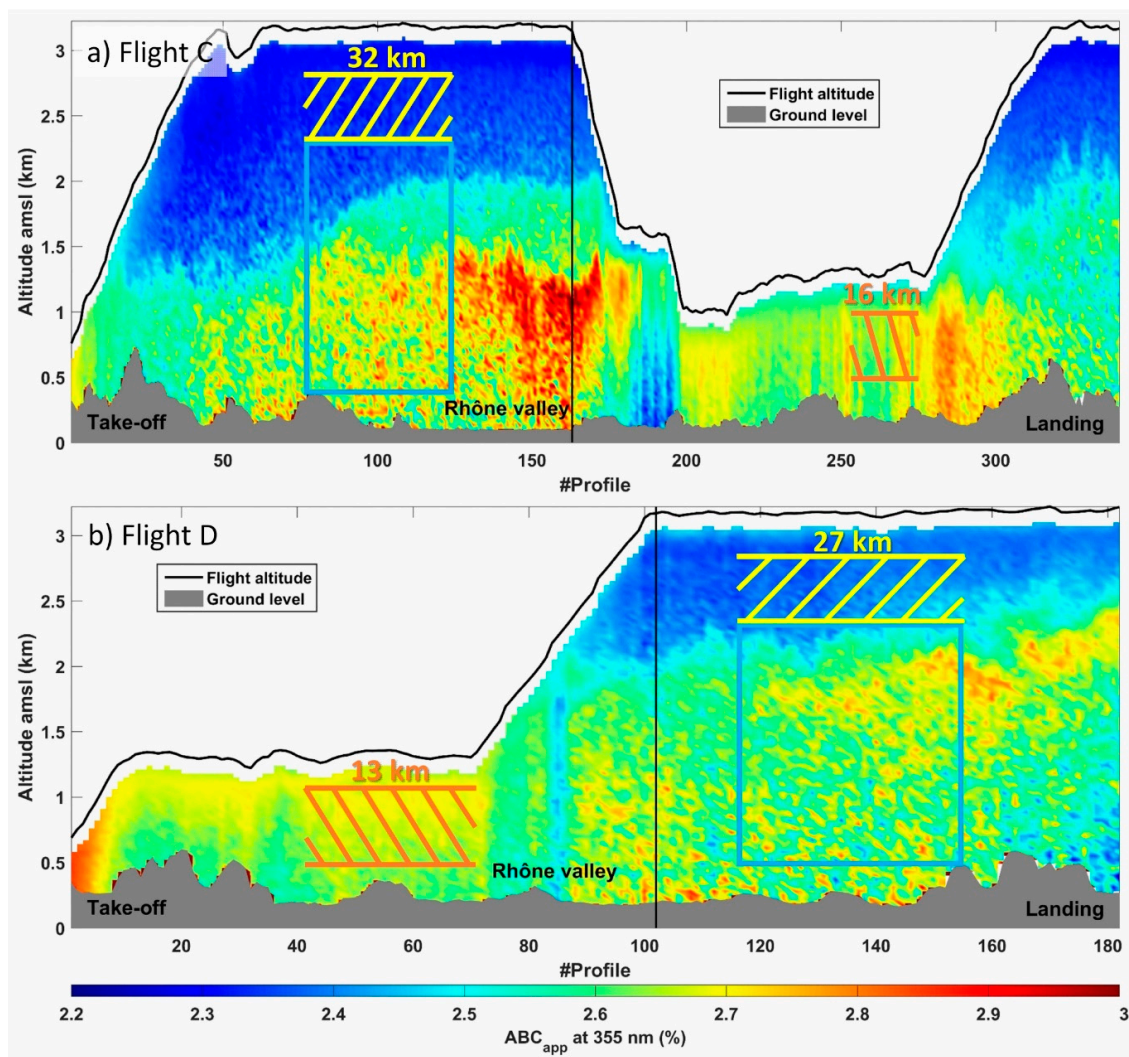


**Figure 8.** Vertical profiles of the normalized apparent backscatter coefficient ( $ABC_{app}$ ) corrected for the molecular transmission for: (a) flight C and (b) flight D on 24 June 2015. Profile number (i.e., time) is indicated in abscise. The profiles used for the study are hatched in orange for the constraint zone between 0.5 and 1 km amsl and yellow for the reference zone between 2.35 and 2.85 km amsl. The inverted profiles are framed in blue. The horizontal distances over which these signals are averaged are indicated.

### 3.2.2. Inversion

The inversion algorithm is applied on average profiles calculated over the areas framed in blue in Figures 7 and 8. Results are presented in Figure 9 for flights C and D. For flight C, the profile is averaged over 41 sequences of 400 laser shots so that the SNR reaches 10 in both the constraint and reference zones. In the case of flight D, the number of available profiles is lesser, and only 31 sequences could be considered. The inversion converged on all sequences of both flights. The AEC determined in the reference zone is not null and is similar for both flights. The retrieved LRs of flights C ( $LR = 31 \pm 8$  sr) and D ( $LR = 54 \pm 7$  sr) encompass those of flights A and B. We note that the PDR remains stable in the PBL for all the flights, with values ranging from 2% to 4%, but associated with an absolute uncertainty at least 2%. There seems to be more terrigenous particles in the aerosol mix of the PBL during flight C performed at the beginning of the afternoon.

The vertical profiles of AEC above are compared to those deduced from horizontal measurements made over Aubenais airfield. We find a very good match in the PBL, but a significant discrepancy

in the lower free troposphere, between 1.5 and 2.5 km amsl. This difference may be due to the large fractionated cloud layer encountered right above the Aubenas area. Locally hydrated aerosols could bias AECs derived from horizontal measurements, just like during flight A. Nevertheless, the comparison of the two methods is satisfactory and corroborates the algorithm proposed for the optimal use of the N<sub>2</sub>-Raman channel. A detailed study of the error budget in the next section will validate this conclusion.

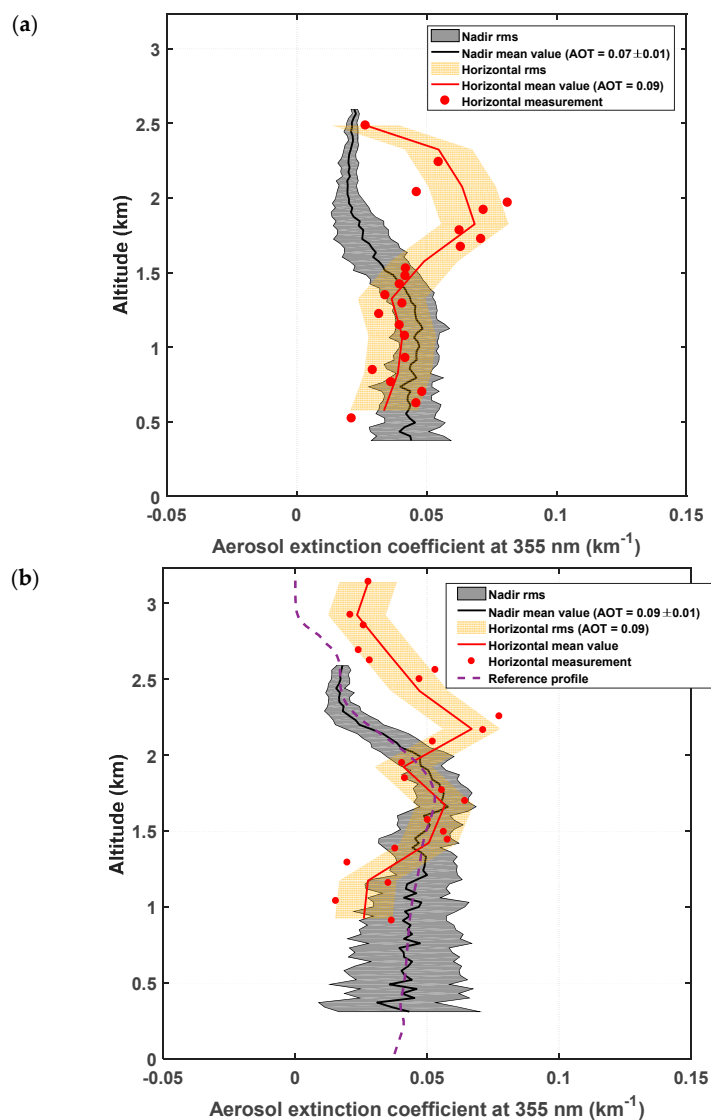


**Figure 9.** Vertical profile of the aerosol extinction coefficient derived from the vertical (grey area) and horizontal (orange area) Lidar measurements for: (a) flight C and (b) flight D on 24 June 2015. The reference profile used for the error budget is shown in (b) by a purple line.

## 4. Error Budget

### 4.1. Uncertainty Sources

Six main sources of uncertainty influence the Lidar ratio and the vertical profile of the AEC retrieved from the airborne N<sub>2</sub>-Raman Lidar: (i) the uncertainty in the a priori knowledge of the vertical profile of the molecular backscatter coefficient; (ii) the uncertainty in the Ångström exponent, (iii) the uncertainty in the range-corrected Lidar signal in the altitude interval used for the normalization; (iv) the uncertainty in the AOT used as a constraint in the PBL; (v) the natural variability of the

atmosphere during the flight; and (vi) the shot noise. In the following, these sources will be considered as independent.

The bias on the a priori knowledge of the molecular contribution has been assessed to be lower than 2% [42] using a comparison between several vertical radio soundings, and it is not dominant in the error budget. The effects of each of the other uncertainty sources over the retrieved optical aerosol properties have been assessed using a Monte Carlo approach, like the one described by Chazette et al. [43].

#### 4.2. Input Conditions for Simulations

The input conditions for the simulations are given by the AEC vertical profile plot in Figure 9b (reference profile in dotted line), and a chosen constant LR value of 55 sr, yielding a total AOT of 0.11 at 355 nm. This value is relatively small, but close to our observations. Note that the increase of the total AOT does not significantly change the conclusions below, where a low AOT is a rather unfavorable condition. The range-corrected Lidar signals are computed in such a way that the SNR for each channel matches the one observed during the measurements. The calculation is carried out for 31 sequences of 400 laser shots, corresponding to a total of 12,400 shots, and a vertical resolution of 30 m. This corresponds to a temporal resolution of ~11 min, and thus a distance of ~16 km along the ground track of a ULA-carrier. The flight altitude is chosen to be 3.2 km amsl.

During the flights on 21 June, little information is available on the Ångström exponent. The AERONET stations of Toulon and Observatoire de Haute Provence (OHP), in the vicinity of the experiment, measured values of 1.26 and 1.41, respectively. For the simulations, we arbitrarily choose a value of 1 with possible biases of  $\pm 0.5$ .

For the Monte Carlo process, a Gaussian draw of 500 random noisy Lidar profiles is performed using the estimated SNR values for each channel. The SNR mainly represents the effect of the shot noise. It is always larger than 10 on the elastic channel. It is less than 10 under 2.4 km amsl, ~0.8 km away from the Lidar, on the  $N_2$ -Raman channel. An example of random draws is given in Figure 10 for the two channels. The reference zone is associated with a scattering ratio of 1.028.

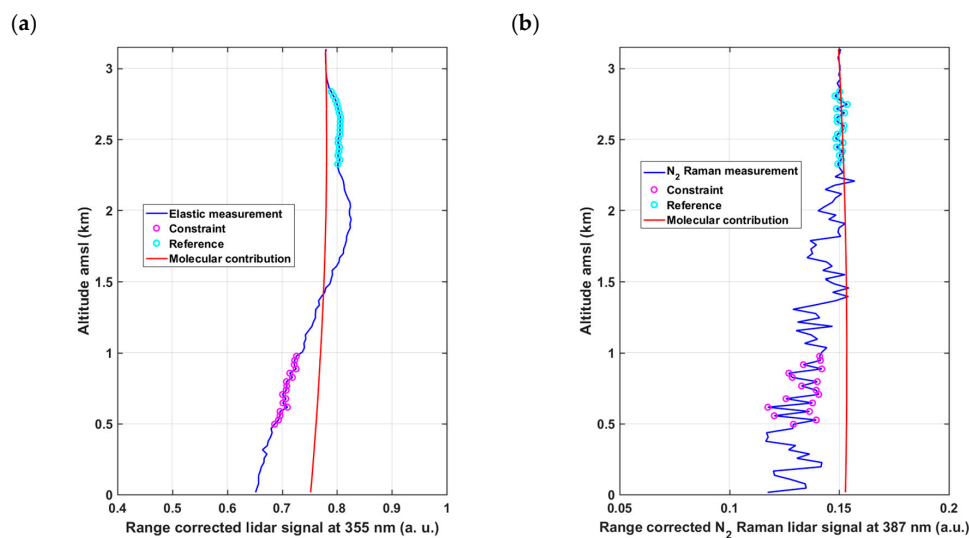


**Figure 10.** Example of random draws used for the Monte Carlo approach for: (a) the elastic channel and (b) the  $N_2$ -Raman channel. The reference altitude interval (2.35–2.85 km amsl) is given by turquoise circles and the constraint altitude interval (0.5–1 km amsl) is given by purple circles. A purely molecular Lidar signal is drawn as a continuous red line.

### 4.3. Results of the Error Budget

#### 4.3.1. Error Due to Shot Noise and Reference AOT Estimation (Fixed Constraint AOT)

In general, the range-corrected Lidar profiles are normalized in a reference zone deemed to be free from aerosols. This is not always true, mainly because airborne measurements and strong biases can be encountered in Lidar ratio and AOT with such a hypothesis [22]. With the proposed algorithm, the AOT in the reference zone is first assessed with the N<sub>2</sub>-Raman channel and the mean ABC at the reference altitude. The LRs are then simultaneously assessed using the AOT from the constraint zone. In this sub-section, only the effect of the shot noise on the Lidar signal and, in particular, in the reference zone, is taken into account on the AOT. The AOT of the constraint zone (~0.018) is assumed to be known.

The results of the Monte Carlo simulation are given in Table 4. The total uncertainty on the LR is 4.2 sr and the total relative uncertainty on the total AOT is ~10%, mainly due to rms error. The reference AOT is known only within ~40% due to shot noise, but remains weak. The vertical profile of the AEC is shown in Figure 11a. The rms increases gradually with distance from the Lidar to reach ~30% close to the ground. The inversion, which is normally unstable, is strongly stabilized by the constraint on the AOT in the PBL. Without this constraint, the inversion does not converge in such noise condition.

**Table 4.** Results of the Monte Carlo approach in terms of bias, standard deviation (rms) and total uncertainty for the AOT (i) at the reference (AOT<sub>r</sub>); (ii) for the total vertical profile (AOT<sub>t</sub>); (iii) at the constraint zone (AOT<sub>c</sub>), as well as for the Lidar ratio (LR). When useful, we also indicate in italic type whether the inversion is carried out with one or two levels of flight.

Condition	Variable (Value)	Bias	Standard Deviation (rms)	Total Uncertainty (Relative)
<b>Airborne N<sub>2</sub>-Raman Lidar</b>				
Unknown AOT <sub>r</sub> & known AOT <sub>c</sub> . <i>2 levels of flight</i>	AOT <sub>r</sub> (0.008)	0	0.003	0.003 (37.5%)
	AOT <sub>t</sub> (0.11)	+0.002	0.012	0.013 (11.1%)
	LR (55 sr)	+2.9 sr	3.1 sr	4.2 sr (7.6%)
Unknown AOT <sub>r</sub> & AOT <sub>c</sub> . <i>2 levels of flight</i>	AOT <sub>r</sub> (0.008)	0	0.003	0.003 (37.5%)
	AOT <sub>t</sub> (0.11)	+0.003	0.014	0.014 (12.7%)
	LR (55 sr)	-2.3 sr	22.2 sr	22.3 sr (40.6%)
Unknown Ångström (1 ± 0.5) (no rms)	AOT <sub>t</sub> (0.11)	±0.001	-	0.001 (1%)
	LR (55 sr)	±1.5 sr	-	1.5 sr (2.7%)
Vertical resolution from 0.75 to 30 m (no rms)	AOT <sub>t</sub> (0.11)	+0.005	-	0.005 (4.5%)
	LR (55 sr)	+1.5 sr	-	1.5 sr (2.7%)
<b>Lidar with 90 mJ Emittted Energy without Loss</b>				
Constraint zone (0.5–1 km amsl) <i>2 levels of flight</i>	AOT <sub>r</sub> (0.008)	0	0.001	0.001 (12.5%)
	AOT <sub>t</sub> (0.11)	0.003	0.005	0.006 (5.5%)
	AOT <sub>c</sub> (0.02)	-	0.003	0.003 (16%)
	LR (55 sr)	3.3 sr	1.4 sr	3.6 sr (6.4%)
Constraint zone (0.5–1 km amsl) <i>1 level of flight</i>	AOT <sub>r</sub> (0.008)	0.0	0.001	0.001 (12.5%)
	AOT <sub>t</sub> (0.11)	0.0012	0.018	0.018 (16.4%)
	AOT <sub>c</sub> (0.02)	-0.001	0.005	0.005 (25%)
	LR (55 sr)	1.3 sr	7.7 sr	7.8 sr (14.1%)
Constraint zone (0.5–2 km amsl) <i>1 level of flight</i>	AOT <sub>r</sub> (0.008)	0	0.001	0.001 (12.5%)
	AOT <sub>t</sub> (0.11)	-0.001	0.008	0.008 (7.3%)
	AOT <sub>c</sub> (0.07)	0.0	0.004	0.004 (5.7%)
	LR (55 sr)	2.2 sr	2.0 sr	3.0 sr (5.4%)

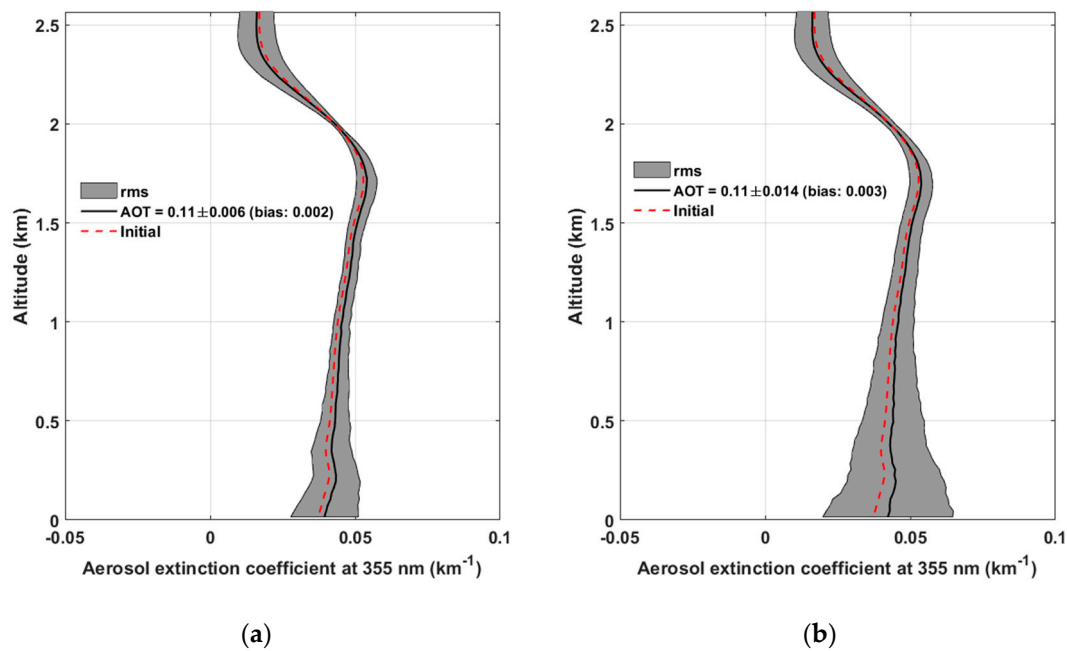


**Figure 11.** Vertical profiles of the aerosol extinction coefficient (AEC) retrieved using the Monte Carlo approach for: (a) the effect of uncertainty over the reference zone and (b) the simultaneously effects of uncertainties over the reference and constraint zones. The “true” input profile is given by the red dotted line; the mean AEC retrieval is given by the black continuous line. The standard deviation (rms) is highlighted in gray.

#### 4.3.2. Error Due to Shot Noise, Reference, and Constraint AOT Estimations

In this sub-section, we add the uncertainty over the constraint AOT to previous calculations. To evaluate the rms error on the signal in the constraint zone, a segment of flight D with the carrier flying at  $\sim 1.3$  km amsl was used. This error thus includes the effect of shot noise, but also that of the natural variability of the atmosphere. The constraint AOT, calculated between 0.5 and 1 km amsl, was thus determined from the  $N_2$ -Raman channel with a relative standard deviation of 16% on an ensemble of 25 significant profiles, corresponding to an absolute error of 0.003. It is this value that is used in the following.

The results of the Monte Carlo approach are also given in Table 4. The total uncertainty on the LR is greatly increased; it reaches  $\sim 22$  sr, but the one on the total AOT remains at 0.014 (13%). The proposed algorithm leads to a stability of the results via an adjustment of the LR. The rms error on the vertical profile of the AEC increases, as shown in Figure 11b. Note that the observed shape of the rms envelope (in gray) is due to the effect of the compensation linked to the constraint on the AOT in the PBL. The rms error on the AEC near the ground level is high, reaching a 50% relative value. To decrease this effect, the Lidar characteristics must be improved. Nevertheless, these simulations validate the levels of uncertainty of the experimental results presented in Figures 5 and 9.

#### 4.3.3. Error Due to the Ångström Exponent

Because it intervenes directly in the calculation of the constraint AOT at 355 nm, a poor knowledge of the value of the Ångström coefficient may induce important biases in the proposed inversion method. For this algorithm, the AOT biases due to errors on the Ångström exponent will be compensated by an adjustment of LR, as shown in the previous sub-section. We have applied Ångström errors of  $\pm 0.5$  to quantify their effects on aerosol optical properties, as reported in Table 4. The biases exerted on AOT and LR remain low, less than 0.005 (4.5%) and 1.5 sr ( $\sim 3\%$ ) respectively. Thus, Ångström exponent is not a predominant source of error, thanks to the proximity of the emission and Raman wavelengths.

Additionally, it should be noted that the biases given in Table 4 include those due to the change in vertical resolution before the inversion. Indeed, to improve SNR, we degrade vertical resolution from 0.75 m to 30 m for our study, also setting a lower limit on the thickness of the reference and constraint zones. Although weak, the effect of this procedure is a bias of +4.5% on total AOT and a bias of +1.5 sr on LR. They may be partly compensated in the highly nonlinear inversion algorithm as they are integrated in the previous results, but remain interesting to consider as a floor value in the error budget.

#### 4.4. Extrapolation towards a Future Airborne N<sub>2</sub>-Raman Lidar

As previously explained, for the simulation above, the noise levels matched those observed on the ULA-carried Lidar. However, during the campaign, the SNR observed during the high-altitude segments of the flights (~3 km amsl) was lower than expected. This is due to a loss of laser pulse energy in the frequency tripling stage, linked to a strong cooling from the relative wind at high altitude, as the Lidar was insufficiently insulated. This energy loss is easily evaluated by comparing raw signals at various carrier altitudes, waiting for stabilization at each stage. The result is a fall of nearly 39% compared to ground level, which has been taken into account as well as in our error budget. Knowing that SNR varies according to the root of the laser pulse energy, the consequence of this effect on the error budget is only marginal.

However, a proper evaluation, without this 39% loss and assuming a powerful, transportable, eye-safe and commercially available laser, needs to be performed in order to assess the potential of an airborne N<sub>2</sub>-Raman Lidar system in optimal conditions, which should be the case in a research plane. We will thus extrapolate the above error budget in the case of a Raman Lidar emitting 90 mJ at 355 nm, with a 20 Hz pulse repetition frequency. Such a laser remains suitable for a plane in terms of size and required power supply, and achieves eye-safety for a beam size of ~50 mm.

Two simulations are performed. The first replicates the same flight protocol that was used with the ULA. The second assumes a single average profile obtained from a high-altitude segment at ~3 km amsl, hoping that the Raman maximum range can be sufficient to reach the constraint zone below 1 km amsl. Indeed, in that case, the Raman channel SNR is significantly enhanced to above 20 within 1 km of the plane carrier. The uncertainty over the reference AOT goes down from 40% to only 10%.

The results of these two simulations are reported in the bottom part of Table 4 and in Figure 12. Considering flight plans like those performed during this campaign, the precision on retrieved parameters is expectedly much better. Both LR and total AOT are estimated with a total relative uncertainty of 6%. However, in the case of the second simulation with a constraint obtained from a single average Lidar profile measured from a high altitude, the uncertainty is higher and reaches about 15%. This still remains reasonable given the airborne measurement conditions, and could be reduced with longer integration to the cost of worsening horizontal resolution. One could also widen the constraint zone towards higher altitudes, which would also decrease rms error on the constraint AOT. In Table 4, such a zone from 0.5 to 2 km amsl has also been tested to set the constraint. This leads to a sharp decrease in error and matches the first simulation with two altitude levels and 90 mJ emitted energy. The retrieved AEC vertical profile is similar to that of Figure 12a.

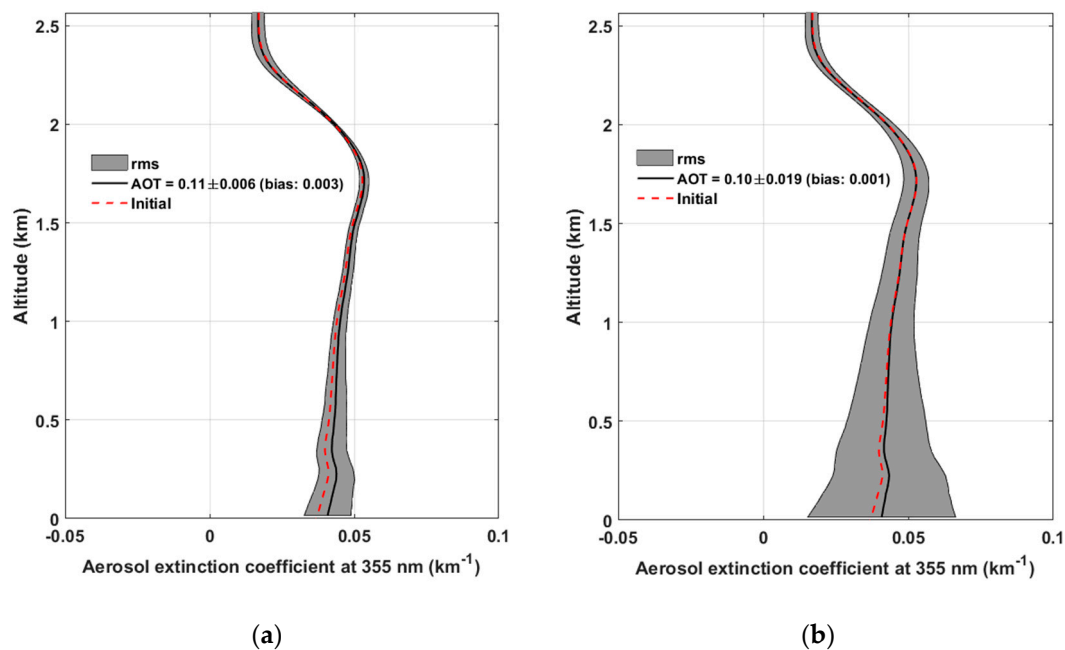


**Figure 12.** Vertical profiles of the aerosol extinction coefficient (AEC) retrieved using the Monte Carlo approach for flight strategies: (a) on two flight altitude levels and (b) on a single flight altitude level. The initial value is given by the red dotted line, the mean AEC retrieval is given by the black continuous line. The standard deviation (rms) is highlighted in gray.

## 5. Conclusions

In the framework of a specific airborne experiment in June 2015, we have proposed a flight strategy using a ULA and the associated inversion algorithm, so as to test the potential of a N<sub>2</sub>-Raman Lidar system to study aerosols in the low and middle troposphere. The existing Lidar system was previously involved with success in several ground based campaigns [6,44]. Additionally, for several years, ULA carriers have been used for various scientific applications [15]. Flying a Raman Lidar on a ULA, although challenging in terms of size and signal processing, seemed completely realistic. We have thus tested this new payload over the Rhône valley, taking off from Aubenais airfield (44.54° N, 4.37° E).

These tests, despite the limited range of the N<sub>2</sub>-Raman channel during the daytime, have proven highly conclusive. To compensate for the lack of power and the possible presence of aerosols at the flight altitude, after evaluating the Lidar overlap factors via horizontal measurements while spiraling up, we have set up a flight scenario split into two altitude levels. This scenario allows the Raman channel to measure residual AOTs in the reference zone used to normalize the Lidar signal, and in a constraint zone within the PBL used to stabilize the notoriously unstable top-down inversion process. The different flights have allowed for comparing the results of the proposed algorithm, in terms of retrieved Lidar ratio (LR) and aerosol extinction (AEC) profile, to a validated approach using horizontal measurements [37]. They were also used to calibrate noise levels for a realistic Monte Carlo simulation. Thanks to the simulation, we were able to evaluate the uncertainties associated to an inversion algorithm immune to an aerosol-contaminated reference zone (see Table 4). The use of a low altitude constraint zone in this algorithm does stabilize the solution in terms of retrieved AOT (no convergence without it).

From the simulation tool with noise included, calibrated on the encountered airborne observations, other measurement scenarios can be imagined and tested. Given the conditions recorded in the field, we have estimated the performances of an optimal airborne Raman Lidar system. We show that, with the Lidar characteristics from Table 3 and a laser pulse energy of 90 mJ (20 Hz PRF), the system is

suitable for airborne science operations to study the low and middle troposphere. Relative uncertainties on LR are about 5 to 6%, whereas uncertainties on the total AOT are around 7%. With this type of laser, the payload remains reasonable in terms of power requirements, size and weight, so as to complement the equipment usually put onboard atmospheric research aircrafts [13,20,22,45].

**Acknowledgments:** This work was supported by the French Institut National de l'Univers (INSU) of the Centre National de la Recherche Scientifique (CNRS) via the French Arctic initiative. The French space agency (CNES) and the Commissariat à l'Énergie Atomique et aux énergies alternatives (CEA) are acknowledged for their support. The ULA flights were performed by Franck Toussaint. The Air Creation Company is acknowledged for its hospitality. The authors acknowledge the MODIS Science, Processing and Data Support Teams for producing and providing MODIS data (<https://modis.gsfc.nasa.gov/data/dataproduct/>). The European Organisation for the Exploitation of Meteorological Satellites (EUMETSAT) is acknowledged for producing and providing SEVIRI data.

**Author Contributions:** Patrick Chazette conceived, designed the experiments and analyzed the data. He developed the algorithm. Julien Totems prepared and participated in the experiment. Both authors wrote the paper.

**Conflicts of Interest:** The authors declare no conflict of interest.

## References

1. IPCC. *Climate Change 2014: Impacts, Adaptation, and Vulnerability. Part A: Global and Sectoral Aspects. Contribution of Working Group II to the Fifth Assessment Report of the Intergovernmental Panel on Climate Change*; Field, C.B., Barros, V.R., Dokken, D.J., Mach, K.J., Mastrandrea, M.D., Bilir, T.E., Chatterjee, M., Ebi, K.L., Estrada, Y.O., Genova, R.C., Eds.; Cambridge University Press: Cambridge, UK; New York, NY, USA, 2014.
2. Le-Treut, H.; Somerville, R.; Cubasch, U.; Ding, Y.; Mauritzen, C.; Mokssit, A.; Peterson, T.; Prather, M.; Qin, D.; Manning, M.; et al. Historical Overview of Climate Change Science. In *Climate Change 2007: The Physical Science Basis*; Cambridge University Press: Cambridge, UK, 2007; Chapter 1, pp. 93–127.
3. Ramanathan, V.; Crutzen, P.J.; Kiehl, J.T.; Rosenfeld, D. Aerosols, climate, and the hydrological cycle. *Science* **2001**, *294*, 2119–2124. [[CrossRef](#)] [[PubMed](#)]
4. Hodzic, A.; Vautard, R.; Chepfer, H.; Goloub, P.; Menut, L.; Chazette, P.; Deuzé, J.L.; Apituley, A.; Couvert, P. Evolution of aerosol optical thickness over Europe during the August 2003 heat wave as seen from CHIMERE model simulations and POLDER data. *Atmos. Chem. Phys.* **2006**, *6*, 1853–1864. [[CrossRef](#)]
5. Tombette, M.; Chazette, P.; Sportisse, B.; Roustan, Y. Simulation of aerosol optical properties over Europe with a 3-D size-resolved aerosol model: Comparisons with AERONET data. *Atmos. Chem. Phys.* **2008**, *8*, 7115–7132. [[CrossRef](#)]
6. Royer, P.; Chazette, P.; Sartelet, K.; Zhang, Q.J.; Beekmann, M.; Raut, J.-C. Comparison of Lidar-derived PM<sub>10</sub> with regional modeling and ground-based observations in the frame of MEGAPOLI experiment. *Atmos. Chem. Phys.* **2011**, *11*, 10705–10726. [[CrossRef](#)]
7. Wang, Y.; Sartelet, K.N.; Bocquet, M.; Chazette, P.; Sicard, M.; D'Amico, G.; Léon, J.F.; Alados-Arboledas, L.; Amodeo, A.; Augustin, P.; et al. Assimilation of Lidar signals: Application to aerosol forecasting in the western Mediterranean basin. *Atmos. Chem. Phys.* **2014**, *14*, 12031–12053. [[CrossRef](#)]
8. Kaufman, Y.J.; Hobbs, P.V.; Kirchhoff, V.W.J.H.; Artaxo, P.; Remer, L.A.; Holben, B.N.; King, M.D.; Ward, D.E.; Prins, E.M.; Longo, K.M.; et al. Smoke, Clouds, and Radiation-Brazil (SCAR-B). *J. Geophys. Res.* **1998**, *103*, 31783–31808. [[CrossRef](#)]
9. Russell, P.B.; Hobbs, P.V.; Stowe, L.L. Aerosol properties and radiative effects in the United States East Coast haze plume: An overview of the Tropospheric Aerosol Radiative Forcing Observational Experiment (TARFOX). *J. Geophys. Res.* **1999**, *104*, 2213–2222. [[CrossRef](#)]
10. Raes, F.; Bates, T.; McGovern, F.; Van Liedekerke, M. The 2nd Aerosol Characterization Experiment (ACE-2): General overview and main results. *Tellus B* **2000**, *52*, 111–125. [[CrossRef](#)]
11. Ramanathan, V.; Crutzen, P.J.; Lelieveld, J.; Mitra, A.P.; Althausen, D.; Anderson, J.; Andreae, M.O.; Cantrell, W.; Cass, G.R.; Chung, C.E.; et al. Indian Ocean Experiment: An integrated analysis of the climate forcing and effects of the great Indo-Asian haze. *J. Geophys. Res. Atmos.* **2001**, *106*, 28371–28398. [[CrossRef](#)]

12. Vautard, R.; Menut, L.; Beekmann, M.; Chazette, P.; Flamant, P.H.; Gombert, D.; Guédalia, D.; Kley, D.; Lefebvre, M.-P.; Martin, D.; et al. A synthesis of the Air Pollution Over the Paris Region (ESQUIF) field campaign. *J. Geophys. Res.* **2003**, *108*. [[CrossRef](#)]
13. Freney, E.J.; Sellegri, K.; Canonaco, F.; Colomb, A.; Borbon, A.; Michoud, V.; Doussin, J.-F.; Crumeyrolle, S.; Amarouche, N.; Pichon, J.-M.; et al. Characterizing the impact of urban emissions on regional aerosol particles: Airborne measurements during the MEGAPOLI experiment. *Atmos. Chem. Phys.* **2014**, *14*, 1397–1412. [[CrossRef](#)]
14. Flamant, C.; Chaboureaud, J.P.; Parker, D.J.; Taylor, C.M.; Cammas, J.P.; Bock, O.; Timouk, F.; Pelon, J. Airborne observations of the impact of a convective system on the planetary boundary layer thermodynamics and aerosol distribution in the inter-tropical discontinuity region of the West African Monsoon. *Q. J. R. Meteorol. Soc.* **2007**, *133*, 1175–1189. [[CrossRef](#)]
15. Raut, J.-C.; Chazette, P. Radiative budget in the presence of multi-layered aerosol structures in the framework of AMMA SOP-0. *Atmos. Chem. Phys.* **2008**, *8*, 12461–12528. [[CrossRef](#)]
16. Formenti, P.; Rajot, J.L.; Desboeufs, K.; Saïd, F.; Grand, N.; Chevaillier, S.; Schmechtig, C. Airborne observations of mineral dust over western Africa in the summer Monsoon season: Spatial and vertical variability of physico-chemical and optical properties. *Atmos. Chem. Phys.* **2011**, *11*, 6387–6410. [[CrossRef](#)]
17. Johnson, B.T.; Heese, B.; McFarlane, S.A.; Chazette, P.; Jones, A.; Bellouin, N. Vertical distribution and radiative effects of mineral dust and biomass burning aerosol over West Africa during DABEX. *J. Geophys. Res.* **2008**, *113*. [[CrossRef](#)]
18. DeCarlo, P.F.; Dunlea, E.J.; Kimmel, J.R.; Aiken, A.C.; Sueper, D.; Crouse, J.; Wennberg, P.O.; Emmons, L.; Shinozuka, Y.; Clarke, A.; et al. Fast airborne aerosol size and chemistry measurements above Mexico City and Central Mexico during the MILAGRO campaign. *Atmos. Chem. Phys.* **2008**, *8*, 4027–4048. [[CrossRef](#)]
19. Molina, L.T.; Madronich, S.; Gaffney, J.S.; Apel, E.; de Foy, B.; Fast, J.; Ferrare, R.; Herndon, S.; Jimenez, J.L.; Lamb, B.; et al. An overview of the MILAGRO 2006 Campaign: Mexico City emissions and their transport and transformation. *Atmos. Chem. Phys.* **2010**, *10*, 8697–8760. [[CrossRef](#)]
20. Ancellet, G.; Pelon, J.; Blanchard, Y.; Quennehen, B.; Bazureau, A.; Law, K.S.; Schwarzenboeck, A. Transport of aerosol to the Arctic: Analysis of CALIOP and French aircraft data during the spring 2008 POLARCAT campaign. *Atmos. Chem. Phys.* **2014**, *14*, 8235–8254. [[CrossRef](#)]
21. Marengo, F.; Johnson, B.; Turnbull, K.; Newman, S.; Haywood, J.; Webster, H.; Ricketts, H. Airborne Lidar observations of the 2010 Eyjafjallajökull volcanic ash plume. *J. Geophys. Res.* **2011**, *116*, D00U05. [[CrossRef](#)]
22. Chazette, P.; Dabas, A.; Sanak, J.; Lardier, M.; Royer, P. French airborne Lidar measurements for Eyjafjallajökull ash plume survey. *Atmos. Chem. Phys.* **2012**, *12*, 7059–7072. [[CrossRef](#)]
23. Shipley, S.T.; Tracy, D.H.; Eloranta, E.W.; Trauger, J.T.; Sroga, J.T.; Roesler, F.L.; Weinman, J.A. High spectral resolution Lidar to measure optical scattering properties of atmospheric aerosols 1: Theory and instrumentation. *Appl. Opt.* **1983**, *22*, 3716–3724. [[CrossRef](#)] [[PubMed](#)]
24. Heaps, W.S.; Burris, J. Airborne Raman Lidar. *Appl. Opt.* **1996**, *35*, 7128–7135. [[CrossRef](#)] [[PubMed](#)]
25. Whiteman, D.N.; Schwemmer, G.; Berkoff, T.; Plotkin, H.; Ramos-Izquierdo, L.; Pappalardo, G. Performance modeling of an airborne Raman water-vapor Lidar. *Appl. Opt.* **2001**, *40*, 375–390. [[CrossRef](#)] [[PubMed](#)]
26. Liu, B.; Wang, Z.; Cai, Y.; Wechsler, P.; Kuestner, W.; Burkhart, M.; Welch, W. Compact airborne Raman Lidar for profiling aerosol, water vapor and clouds. *Opt. Express* **2014**, *22*, 20613–20621. [[CrossRef](#)] [[PubMed](#)]
27. Shang, X.; Chazette, P. End-to-End Simulation for a Forest-Dedicated Full-Waveform Lidar onboard a Satellite Initialized from UV Airborne Lidar Experiments. *Remote Sens.* **2015**, *7*, 5222–5255. [[CrossRef](#)]
28. Klett, J.D. Stable analytical inversion solution for processing Lidar returns. *Appl. Opt.* **1981**, *20*, 211–220. [[CrossRef](#)] [[PubMed](#)]
29. Klett, J.D. Lidar inversion with variable backscatter/extinction ratios. *Appl. Opt.* **1985**, *24*, 1638–1643. [[CrossRef](#)] [[PubMed](#)]
30. Measures, R.M. *Laser Remote Sensing: Fundamentals and Applications*; Wiley, J., Ed.; Krieger Publishing Company: Malabar, FL, USA, 1984.
31. Ansmann, A.; Riebesell, M.; Weitkamp, C. Measurement of atmospheric aerosol extinction profiles with a Raman Lidar. *Opt. Lett.* **1990**, *15*, 746–748. [[CrossRef](#)] [[PubMed](#)]
32. Chazette, P.; Flamant, C.; Shang, X.; Totems, J.; Raut, J.-C.; Doerenbecher, A.; Ducrocq, V.; Fourrié, N.; Bock, O.; Cloché, S. A multi-instrument and multi-model assessment of atmospheric moisture variability over the Western Mediterranean during HyMeX. *Q. J. R. Meteorol. Soc.* **2016**, *142*, 7–22. [[CrossRef](#)]

33. Chazette, P. Exceptional aerosol pollution plume observed using a new ULA-Lidar approach. *Atmos. Environ.* **2016**, *141*, 470–480. [[CrossRef](#)]
34. Royer, P.; Chazette, P.; Lardier, M.; Sauvage, L. Aerosol content survey by mini N2-Raman Lidar: Application to local and long-range transport aerosols. *Atmos. Environ.* **2011**, *45*, 7487–7495. [[CrossRef](#)]
35. Shang, X.; Chazette, P.; Totems, J.; Dieudonné, E.; Hamonou, E.; Duflot, V.; Strasberg, D.; Flores, O.; Fournel, J.; Tulet, P. Tropical Forests of Réunion Island Classified from Airborne Full-Waveform Lidar Measurements. *Remote Sens.* **2016**, *8*, 43. [[CrossRef](#)]
36. Chazette, P. The monsoon aerosol extinction properties at Goa during INDOEX as measured with Lidar. *J. Geophys. Res.* **2003**, *108*, 4187. [[CrossRef](#)]
37. Chazette, P.; Sanak, J.; Dulac, F. New Approach for Aerosol Profiling with a Lidar Onboard an Ultralight Aircraft: Application to the African Monsoon Multidisciplinary Analysis. *Environ. Sci. Technol.* **2007**, *41*, 8335–8341. [[CrossRef](#)] [[PubMed](#)]
38. Chazette, P.; Raut, J.-C.; Dulac, F.; Berthier, S.; Kim, S.-W.; Royer, P.; Sanak, J.; Loaëc, S.; Grigaut-Desbrosses, H. Simultaneous observations of lower tropospheric continental aerosols with a ground-based, an airborne, and the spaceborne CALIOP Lidar system. *J. Geophys. Res.* **2010**, *115*. [[CrossRef](#)]
39. Shang, X.; Chazette, P. Interest of a Full-Waveform Flown UV Lidar to Derive Forest Vertical Structures and Aboveground Carbon. *Forests* **2014**, *5*, 1454–1480. [[CrossRef](#)]
40. Dieudonné, E.; Chazette, P.; Marnas, F.; Totems, J.; Shang, X. Raman Lidar Observations of Aerosol Optical Properties in 11 Cities from France to Siberia. *Remote Sens.* **2017**, *9*, 978. [[CrossRef](#)]
41. Chazette, P.; Totems, J.; Shang, X. Atmospheric aerosol variability above the Paris Area during the 2015 heat wave—Comparison with the 2003 and 2006 heat waves. *Atmos. Environ.* **2017**, *170*, 216–233. [[CrossRef](#)]
42. Chazette, P.; Bocquet, M.; Royer, P.; Winiarek, V.; Raut, J.C.; Labazuy, P.; Gouhier, M.; Lardier, M.; Cariou, J.P. Eyjafjallajökull ash concentrations derived from both Lidar and modeling. *J. Geophys. Res. Atmos.* **2012**, *117*. [[CrossRef](#)]
43. Chazette, P.; Pelon, J.; Mégie, G. Determination by spaceborne backscatter Lidar of the structural parameters of atmospheric scattering layers. *Appl. Opt.* **2001**, *40*, 3428–3440. [[CrossRef](#)] [[PubMed](#)]
44. Dieudonné, E.; Chazette, P.; Marnas, F.; Totems, J.; Shang, X. Lidar profiling of aerosol optical properties from Paris to Lake Baikal (Siberia). *Atmos. Chem. Phys.* **2015**, *15*, 5007–5026. [[CrossRef](#)]
45. Haywood, J.M.; Johnson, B.T.; Osborne, S.R.; Baran, A.J.; Brooks, M.; Milton, S.F.; Mulcahy, J.; Walters, D.; Allan, R.P.; Klaver, A.; et al. Motivation, rationale and key results from the GERBILS saharan dust measurement campaign. *Q. J. R. Meteorol. Soc.* **2011**, *137*, 1106–1116. [[CrossRef](#)]



© 2017 by the authors. Licensee MDPI, Basel, Switzerland. This article is an open access article distributed under the terms and conditions of the Creative Commons Attribution (CC BY) license (<http://creativecommons.org/licenses/by/4.0/>).